

# Hybrid passivated colloidal quantum dot solids

Alexander H. Ip<sup>1†</sup>, Susanna M. Thon<sup>1†</sup>, Sjoerd Hoogland<sup>1</sup>, Oleksandr Voznyy<sup>1</sup>, David Zhitomirsky<sup>1</sup>, Ratan Debnath<sup>1</sup>, Larissa Levina<sup>1</sup>, Lisa R. Rollny<sup>1</sup>, Graham H. Carey<sup>1</sup>, Armin Fischer<sup>1</sup>, Kyle W. Kemp<sup>1</sup>, Illan J. Kramer<sup>1</sup>, Zhijun Ning<sup>1</sup>, André J. Labelle<sup>1</sup>, Kang Wei Chou<sup>2</sup>, Aram Amassian<sup>2</sup> and Edward H. Sargent<sup>1\*</sup>

**Colloidal quantum dot (CQD) films allow large-area solution processing and bandgap tuning through the quantum size effect<sup>1–6</sup>. However, the high ratio of surface area to volume makes CQD films prone to high trap state densities if surfaces are imperfectly passivated, promoting recombination of charge carriers that is detrimental to device performance<sup>7</sup>. Recent advances have replaced the long insulating ligands that enable colloidal stability following synthesis with shorter organic linkers or halide anions<sup>8–12</sup>, leading to improved passivation and higher packing densities. Although this substitution has been performed using solid-state ligand exchange, a solution-based approach is preferable because it enables increased control over the balance of charges on the surface of the quantum dot, which is essential for eliminating midgap trap states<sup>13,14</sup>. Furthermore, the solution-based approach leverages recent progress in metal:chalcogen chemistry in the liquid phase<sup>15–19</sup>. Here, we quantify the density of midgap trap states<sup>20–22</sup> in CQD solids and show that the performance of CQD-based photovoltaics is now limited by electron-hole recombination due to these states. Next, using density functional theory and optoelectronic device modelling, we show that to improve this performance it is essential to bind a suitable ligand to each potential trap site on the surface of the quantum dot. We then develop a robust hybrid passivation scheme that involves introducing halide anions during the end stages of the synthesis process, which can passivate trap sites that are inaccessible to much larger organic ligands. An organic crosslinking strategy is then used to form the film. Finally, we use our hybrid passivated CQD solid to fabricate a solar cell with a certified efficiency of 7.0%, which is a record for a CQD photovoltaic device.**

Using transient photovoltage spectroscopy<sup>23,24</sup> (Fig. 1e) and thermal admittance spectroscopy (Supplementary Section S9), we investigated the trap state densities of the best previously published colloidal quantum dot (CQD) photovoltaic materials: organic crosslinked solids<sup>25</sup> and all-inorganic passivated solids<sup>12</sup>. On illumination of a trap-free p-type semiconductor, the promotion of photoelectrons to the conduction band is followed by rapid thermalization to the band-edge, resulting in an excess free-carrier density that is sustained over the band-to-band lifetime of the charge carriers. This can be envisaged as the establishment of two distinct quasi-Fermi levels, one for electrons and the other for holes, and this separation produces an open-circuit voltage,  $V_{OC}$ . However, when illuminating a semiconductor with trap states in its bandgap, much of the photogenerated charge is instead consumed by filling midgap levels, producing a smaller  $V_{OC}$  for the same photogeneration rate. The photovoltage transient method

directly probes these processes (Fig. 1e). Each studied film exhibited a high density of trap states ( $\sim 1 \times 10^{17} \text{ cm}^{-3} \text{ eV}^{-1}$ ) near the middle of the bandgap (Fig. 1f). A self-consistent simulation of the performance of optoelectronic devices predicts that this density of midgap trap states reduces the power conversion efficiency (PCE) of a photovoltaic device by a factor of two compared with the trap-free case (Fig. 2d; for details of experimental and computational techniques see Methods and the Supplementary Information).

Density functional theory (DFT) was used to explore why such conventional passivation approaches fail to remove midgap traps more completely. We first confirmed that charge balance in the as-synthesized lead-rich surface<sup>26</sup> determines the overall degree of trap passivation (Fig. 1a,b). DFT calculations demonstrated (Fig. 1d) that even a slight imbalance between the number of ligands and the excess lead atoms results in trap states that severely degrade the cleanliness of the bandgap of the quantum solid. Over an entire film, the device performance will suffer dramatically if even a small fraction of quantum dots have just a small number of midgap centres. It is therefore essential that the end-to-end film processing ensures the best possible surface passivation.

DFT was also used to determine whether such complete passivation is feasible using organics alone. It was found that steric considerations prevent organic ligands from penetrating the inter-chain trenches on the surfaces of the quantum dots, causing unpassivated metal surface sites to remain (Fig. 1c). In contrast, halide atoms are compact enough to infiltrate these difficult-to-access sites. Furthermore, halides can be multiply-coordinated with ease, in contrast to the covalent thiol ligands typically used in organic passivation.

In light of these findings, a hybrid passivation scheme was devised aimed at achieving a dramatic improvement in the combination of surface passivation and film density. This scheme uses halide anions in the solution phase to bind hard-to-access sites. At the same time, optimally chosen metal cations are introduced to bind unpassivated surface chalcogens, targeting the removal of valence-band-associated trap states. Finally, during the solid-state film-forming process, bidentate organic linkers are used to maximize packing. Specifically, we introduce a metal halide salt (optimally  $\text{CdCl}_2$  dissolved in a mixture of tetradecylphosphonic acid (TDPA) and oleylamine) during synthesis, immediately following the nucleation and growth of PbS quantum dots. As confirmed by X-ray photoelectron spectroscopy (XPS), Rutherford backscattering spectroscopy (RBS) and inductively coupled plasma atomic emission spectrometry (ICP AES) (Supplementary Sections S1,S2,S5), the halides bind excess surface atoms while displacing a fraction of the oleic acid ligands.

Photoluminescence spectroscopy was used to investigate the impact of halide exposure. Directly after synthesis, both untreated

<sup>1</sup>Department of Electrical and Computer Engineering, University of Toronto, 10 King's College Road, Toronto, Ontario M5S 3G4, Canada, <sup>2</sup>Physical Sciences and Engineering Division, King Abdullah University of Science and Technology (KAUST), Thuwal 23955-6900, Saudi Arabia; <sup>†</sup>These authors contributed equally to this work. \*e-mail: ted.sargent@utoronto.ca

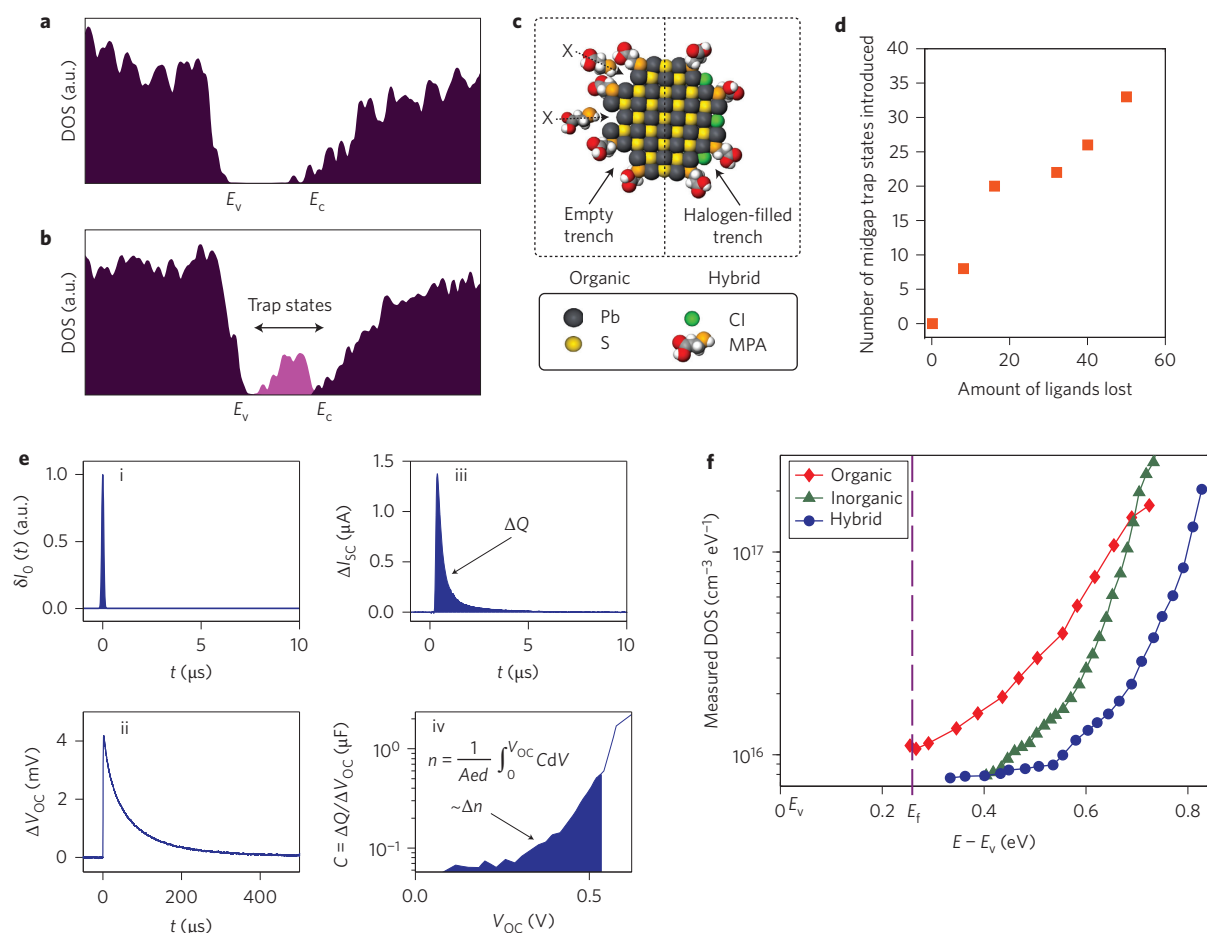


**Figure 1 | Traps in colloidal quantum dot films.** **a**, DFT calculation of the density of states (DOS) for a charge-balanced quantum dot with a clean bandgap. A 2.4 nm PbS quantum dot with the amount of ligands adjusted to provide an ideal electronic balance and close to maximally sterically allowed surface coverage was modelled for the calculation. Note that the obtainable  $V_{OC}$  under illumination is limited by the bandgap for a film made from these quantum dots. **b**, DFT calculation of the DOS for a non-charge-balanced quantum dot (containing half the number of ligands as the quantum dot in **a**), showing a drastic increase in the midgap DOS associated with trap levels (trap states are plotted in light pink). In the case of a film with a significant density of midgap traps, the quasi-Fermi level separation (and therefore  $V_{OC}$ ) under the same illumination is limited by the filling of the midgap states. **c**, Schematic cross-section of a PbS CQD with organic passivation (left) based on MPA, an alkanethiol, and the hybrid passivation scheme (right), in which both MPA and halides are present after solution-phase treatment and solid-state exchange. In the organic case, the MPA molecules are unable to fill all of the inter-atom trenches on the lead-rich surface because of steric considerations (top) or lack of proper coordination number (bottom). In the hybrid case, halogen atoms are small enough to fill the trenches easily and can be multiply coordinated. **d**, Plot of the number of mid-gap trap states introduced as a result of ligands lost from an initially charge-balanced quantum dot. The number of trap states increases in proportion to the number of 'missing' ligands. For the full DOS calculations for the different cases plotted, see Supplementary Section S4. **e**, The photovoltage transient technique. Effect of a light pulse ( $\delta I_0(t)$ ) (i) on the measured change in  $V_{OC}$  (ii) and  $I_{SC}$  (iii) over time. The injected charge  $\Delta Q$  is determined by integrating the current transient. The capacitance (iv) is obtained by dividing  $\Delta Q$  by  $\Delta V$ . The DOS can be calculated by integrating the capacitance over the voltage as shown, where  $n$  is the carrier concentration at each  $V_{OC}$ ,  $A$  is the device area,  $e$  is the electron charge and  $d$  is the film thickness. Details of the calculation can be found in Supplementary Section S6. **f**, DOS in the bandgap calculated from transient photovoltage measurements for organic (red), inorganic (green) and hybrid (blue) passivation of PbS CQD films.

and metal-halide-treated quantum dots have approximately the same solution-phase photoluminescence quantum yield ( $\sim 50\%$ ). However, following the solution-phase washing steps, the photoluminescence quantum efficiency (PLQE) is significantly degraded in conventionally processed nanoparticles as a result of the loss of some oleic acid ligands, but is reduced minimally in the more robust hybrid passivated quantum dots. When the carbon, hydrogen and nitrogen (CHN) content was analysed,  $\text{CdCl}_2$ -treated quantum dots were found to contain 10% less overall carbon and hydrogen compared with PbS-only quantum dots (Supplementary Section S14). This suggests that only the oleic acid passivants (which were presumably in sterically non-ideal locations on the surface) are removed. These are replaced with halide passivants with superior effectiveness (in particular, their small size allows them to tie up hard-to-access surface sites).

We also investigated the composition of films formed from the differently synthesized quantum dots following solid-state treatment using mercaptaptopropionic acid (MPA). It was confirmed that thiols completely displace the original long aliphatic ligands that the halide passivants were unable to remove through the action of the amines alone. Notably, in the final film, the ratio of surface cations to the sum of all ligands (organic plus inorganic) reaches approximately unity (Supplementary Section S3). XPS analysis shows that the same is not true for the organic or inorganic passivation schemes: both are found to have a smaller ligand-to-surface lead ratio than in the hybrid case.

Our hybrid passivation strategy was deployed to build a series of devices in a depleted heterojunction (DH) architecture<sup>2</sup> (Fig. 2a,b). We used a solution-processed n-type electrode that uses a ZnO nanoparticle film deposited on fluorine-doped tin oxide (FTO) as

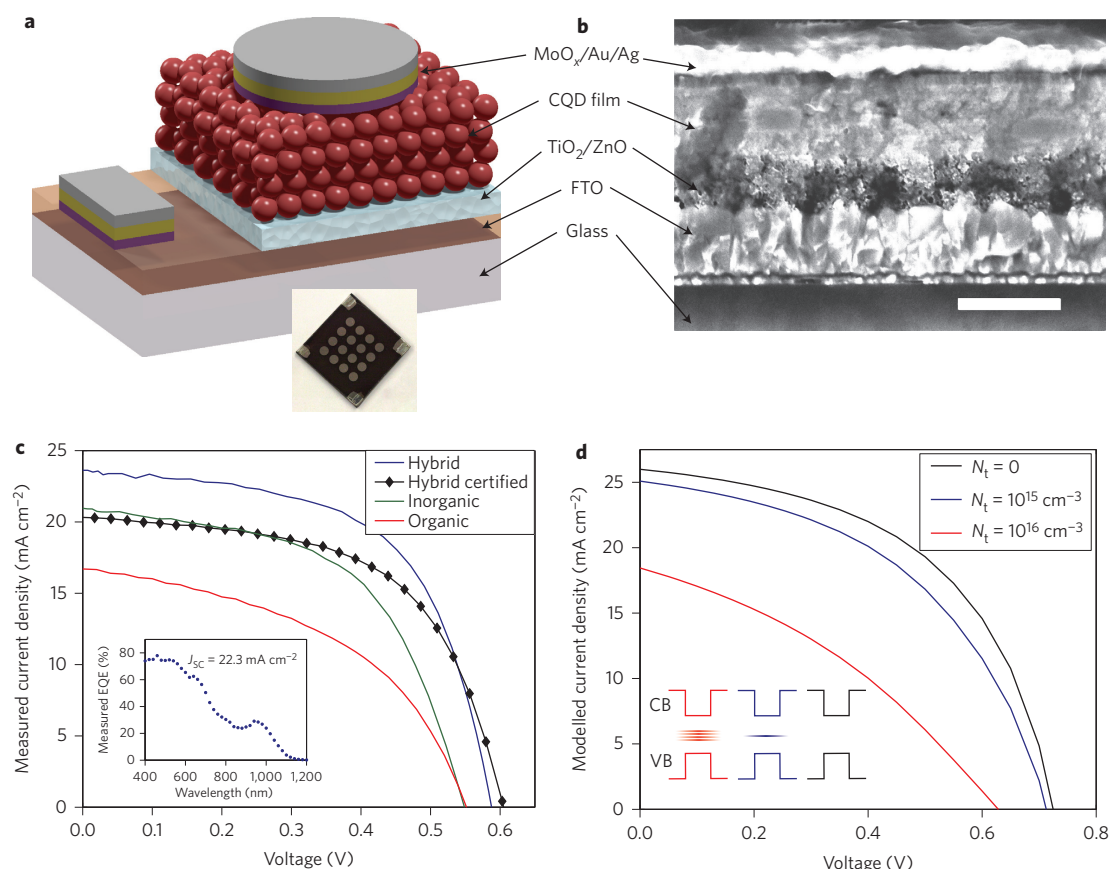


**Figure 2 | Performance of CQD photovoltaics as a function of passivation.** **a**, Schematic of the depleted heterojunction CQD device used in this study. Inset: photograph of a typical device (substrate dimensions, 25 mm × 25 mm). **b**, Cross-sectional SEM image of the same device. Scale bar, 500 nm. **c**, Measured current-voltage characteristics under AM1.5 simulated solar illumination for representative devices employing organic (red), inorganic (green) and hybrid (blue) passivation schemes. Black diamonds are the *J*-*V* curve for a hybrid passivated device as measured by an accredited photovoltaic calibration laboratory (Newport Technology and Application Center-PV Lab). Inset: EQE curve for a hybrid passivated device. The integrated current value is also shown. **d**, Simulated *J*-*V* curves of devices with varying midgap trap densities, demonstrating the detrimental effect of traps.

**Table 1 | Figures of merit for previous record CQD photovoltaic devices compared with the hybrid passivated devices.**

Type	Organic (Ref. 25)	Inorganic (Ref. 12)	Hybrid ( <i>N</i> = 47)
<i>V</i> <sub>oc</sub> (V)	0.56	0.48	0.59 ± 0.01
<i>J</i> <sub>sc</sub> (mA cm <sup>-2</sup> )	17.0	20.2	21.8 ± 0.8
FF (%)	59	62	58 ± 2
PCE (%)	5.6	6.0	7.4 ± 0.3

Statistics for the hybrid case are based on a total of 47 devices prepared on separate substrates.

a template for producing TiO<sub>2</sub> by means of a TiCl<sub>4</sub> treatment<sup>27,28</sup>. Controls using previously published TiO<sub>2</sub> electrodes showed that this minor variation in electrode had little impact on device performance (Supplementary Section S10). We measured the current-voltage characteristics of our hybrid passivated cell in an inert nitrogen environment under 100 mW cm<sup>-2</sup> AM1.5 illumination (Fig. 2c). A photograph of our typical cell layout is shown in the inset in Fig. 2a (typical cell area, 0.049 cm<sup>2</sup>, defined by aperturing during cell measurement). Devices with PCE values of 7% or greater were fabricated on over 40 separate substrates. The average performance of these devices is given in Table 1, and demonstrates a significant performance advance over previously reported organic<sup>25</sup> and inorganic<sup>12</sup> passivated CQD devices. Tests on scaled-up hybrid devices indicate that the current density and voltage can be maintained for areas over 1 cm<sup>2</sup>

(Supplementary Section S11). Using capacitance-voltage measurements, we found the free-carrier densities of all devices shown in Fig. 2c to be between  $1 \times 10^{15}$  and  $1 \times 10^{16}$  cm<sup>-3</sup>, so the enhancement in *V*<sub>OC</sub> cannot be attributed to a difference in doping density alone. The external quantum efficiency (EQE) spectrum (Fig. 2c, inset), when integrated, predicts a current density of 22 mA cm<sup>-2</sup>, consistent with our AM1.5G measurements.

One of our devices measured by an accredited photovoltaics laboratory (Newport Technology and Application Center—PV Lab) was found to display the following figures of merit: open-circuit voltage *V*<sub>OC</sub> = 0.605 V, short-circuit current density *J*<sub>sc</sub> = 20.1 mA cm<sup>-2</sup>, fill factor (FF) = 58% and PCE = 7.0%. This is, to our knowledge, the highest certified PCE reported for a CQD solar cell. Our devices also exhibited relatively good performance stability (less than 15% total PCE degradation over a period of two weeks) when stored in a nitrogen environment (see Supplementary Section S12 for details), which suggests that encapsulated devices will also display promising performance stability.

Transient photovoltage and thermal admittance spectroscopies were used to obtain the midgap trap state density inside the hybrid passivated film. The density was found to be  $2 \times 10^{16}$  cm<sup>-3</sup> eV<sup>-1</sup>, fully five times lower than in conventional organic crosslinked and inorganic-only films (Fig. 1f). This value was inserted into our optoelectronic model, and we found that the improvements in both current and voltage may be explained by our considerably cleaner midgap.

To compare the roles of the metal cation and the halide anion, we also characterized the midgap of films treated with PbCl<sub>2</sub> using the



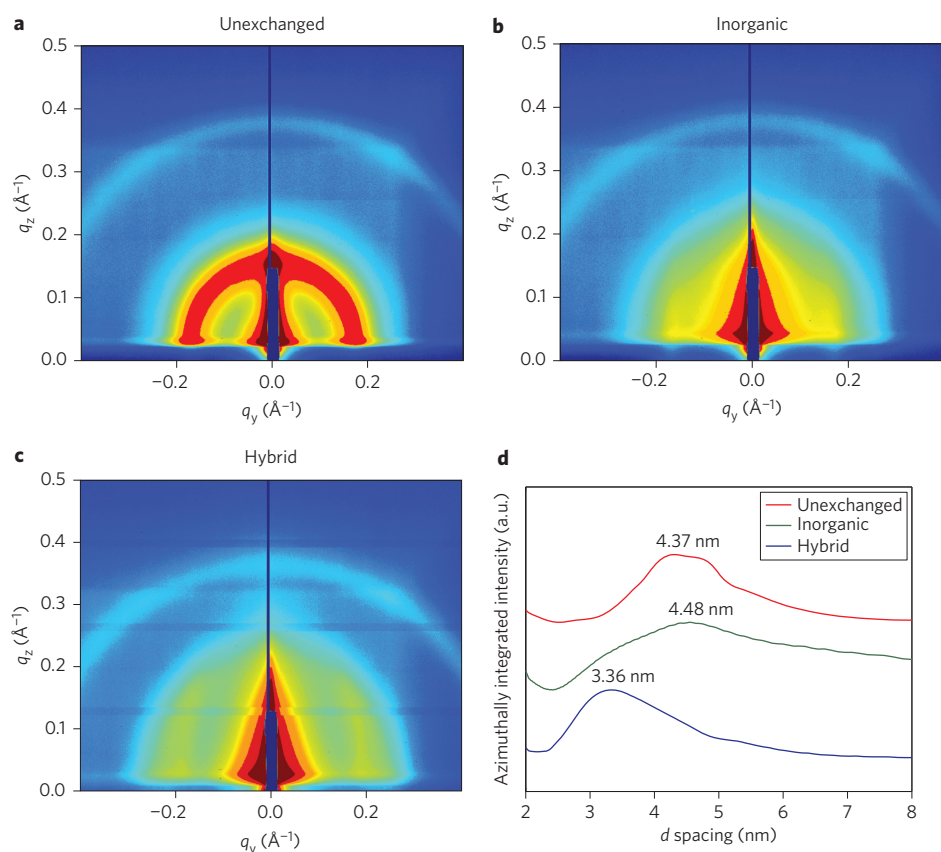


**Figure 3 | Effect of matrix on film density.** **a–c**, GISAXS patterns of as-cast, unexchanged CQDs (**a**) and films treated using fully inorganic passivation following ref. 12 (**b**) and hybrid passivation (**c**). The  $x$ - and  $y$ -axes represent the scattering wave vector in the  $y$  (scattering in the direction along the sample surface perpendicular to the X-ray beam) and  $z$  (scattering normal to the sample surface plane) directions, respectively. The colour scale represents the log of the scattering intensity as recorded by the CCD. Blue represents lower intensity and red represents higher intensity, with each spectrum normalized to show the full dynamic range of each data set. **d**, By integrating the intensity in **a–c** azimuthally, the average interparticle spacing can be found. Inorganic passivation (green curve), in spite of minimally sized atomic ligands, does not increase the film density compared with initially cast dot films (red curve). An exchange using short bidentate organic thiols (blue curve) results in a significant reduction in average interparticle spacing.

same synthesis-phase protocol. These measurements reported a density of trap states in the gap comparable to that of the  $\text{CdCl}_2$ -treated films and a device performance of  $>6\%$  PCE (Supplementary Section S6). We conclude that the halide plays the primary role in midgap trap removal.

We further elucidated the role of each individual constituent in the hybrid approach (Supplementary Section S13). The oleylamine serves to dissolve the metal halide salt and also helps remove synthesis ligands to facilitate the attachment of the halide passivants<sup>15</sup>. The TDPA facilitates binding of the metal cations to the sulphur-rich dot facets, while preventing full cation exchange<sup>29</sup>. Adding a reactive cation complex such as cadmium oleate or cadmium acetate results in the formation of a core-shell structure with an associated increase in  $V_{\text{OC}}$  and a large decrease in  $J_{\text{SC}}$ . Adding tetrabutylammonium chloride, which should contribute only halogens to the dot surface, results in an increase in device performance, and also adding a metal binding complex achieves a device performance nearly equivalent to that of the optimum devices treated with metal halide salts.

We also compared our hybrid approach with a recently reported all-inorganic solid-state approach that achieved a PCE of  $\sim 6\%$  (ref. 12). Synchrotron grazing-incidence small-angle X-ray scattering (GISAXS) measurements were carried out to elucidate the role of the organic ligands<sup>30–32</sup>. GISAXS intensity maps (Fig. 3a–c) revealed the greatest order for the (insulating) oleic-acid-capped quantum dot film. Although the nanoparticles are  $\sim 3.1$  nm in diameter, as seen using transmission electron microscopy

(Supplementary Section S8), GISAXS shows the average centre-to-centre nanocrystal spacing to be 4.4 nm, consistent with the approximately nanometre-scale spacing attributable to bulk oleic acid. When the short bidentate crosslinker MPA was used, the dot spacing was reduced to 3.4 nm. Although their organic content was removed, the all-inorganic films retained a 4.4 nm spacing, with their average centre-to-centre distance unchanged in the solid-state exchange. These findings (Fig. 3d) confirm the important role of the bidentate organic crosslinker in achieving densification at the time of volume contraction during solid-state treatment.

The final aspect of the hybrid scheme is valence band passivation for improved hole mobility. This was achieved by solution-phase metal-cation-based passivation of exposed surface sulphur anions. To study its impact on hole mobility (Fig. 4a–d) we performed time-of-flight (TOF) measurements<sup>10,33</sup> on five different types of film. With no metal halide treatment, the organic crosslinked films had a hole mobility  $\mu_{\text{p}}$  of  $1.0 \times 10^{-3} \text{ cm}^2 \text{ V}^{-1} \text{ s}^{-1}$ , whereas the hybrid film based on  $\text{PbCl}_2$  demonstrated a modestly improved hole mobility of  $\mu_{\text{p}} = 2.6 \times 10^{-3} \text{ cm}^2 \text{ V}^{-1} \text{ s}^{-1}$ . The optimal hybrid film based on  $\text{CdCl}_2$  exhibited the highest hole mobility of  $\mu_{\text{p}} = 4.2 \times 10^{-3} \text{ cm}^2 \text{ V}^{-1} \text{ s}^{-1}$ . We conclude that, although the halide plays a determinative role in midgap state passivation, the choice of cation is important in improving transport associated with the valence band.

The photoluminescence spectra of both the as-synthesized quantum dot solutions and the quantum dot solids reported herein further confirm the effectiveness of the hybrid passivation

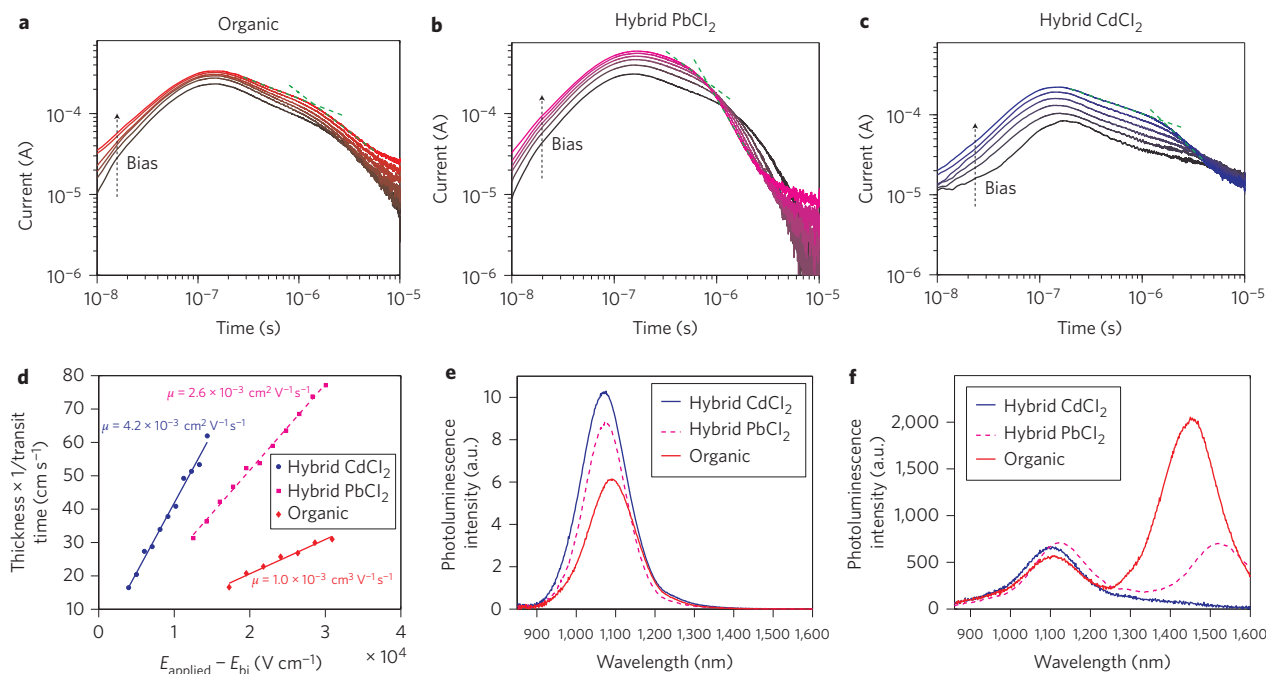


**Figure 4 | Passivation of majority carrier traps via the hybrid method.** **a–c**, TOF measurements showing the hole current versus time (both on log scales) for six different bias voltages between 0 V (bottom line) and 0.6 V (top line, for **a**) or 1 V (top line, for **b** and **c**) for CQD films using organic passivation (**a**), hybrid passivation with a PbCl<sub>2</sub> in-synthesis treatment (**b**) and hybrid passivation using a CdCl<sub>2</sub> in-synthesis treatment (**c**), which we have found to work best in this study. Green lines (only shown for one curve in each panel for clarity) demonstrate the fits to the linear regimes used to extract the carrier transit times. **d**, Extracted carrier velocity plotted versus field to calculate the majority carrier mobility for the organic (red), PbCl<sub>2</sub> hybrid (pink) and CdCl<sub>2</sub> hybrid (blue) cases. A steeper slope (and thus higher mobility) implies improved trap passivation. **e**, Solution-phase photoluminescence intensity of untreated (red), PbCl<sub>2</sub> hybrid (pink) and CdCl<sub>2</sub> hybrid (blue) passivated solutions. Full photoluminescence quantum efficiency measurements indicate a twofold increase in the photoluminescence efficiency of CdCl<sub>2</sub>-treated dots compared with untreated dots (see text for details). **f**, Photoluminescence of organic (red), PbCl<sub>2</sub> hybrid (pink) and CdCl<sub>2</sub> hybrid (blue) passivated films. All films show band-edge photoluminescence, but a marked decrease in trap-associated long wavelength photoluminescence is observed from the organic to the hybrid case, with the CdCl<sub>2</sub> sample showing negligible signal at longer wavelengths.

method. As mentioned above, the solution-phase photoluminescence quantum yield (Fig. 4e) after the washing steps was improved approximately twofold when metal halide treatment was used. The measured photoluminescence efficiencies after methanol washing for the CdCl<sub>2</sub>-treated PbS, PbCl<sub>2</sub>-treated PbS and untreated PbS were 42, 31 and 21%, respectively, whereas the efficiencies before exchange were all between 45 and 50%. MPA-exchanged films made from all three types of dot exhibited band-edge photoluminescence (Fig. 4f) shifted ~150 nm from the excitonic absorption peak. A significant additional feature exists 300–400 nm further to the red in the case of the organic and hybrid PbCl<sub>2</sub>; this can be associated with trap-to-band transitions<sup>34</sup>. The optimized hybrid CdCl<sub>2</sub> consistently showed band-edge-only photoluminescence, consistent with its clear gap both below and above the equilibrium Fermi level.

Our results confirm that, given the diversity of atomic sites present on a quantum dot surface arising as a function of stoichiometry, faceting and initial ligand coverage, a multiple-liganding strategy can be more effective than one based on a single ligand class. Moreover, developing methods to ensure that the bandgap is substantially free of electronic trap states will further enhance the voltage via reduced recombination and improve electrical transport in optoelectronic devices based on CQD solids.

## Methods

**Preparation of metal halide precursors.** Cadmium chloride (Sigma-Aldrich, 99.98%) or lead chloride (Alfa Aesar, 99.999%) and TDPA (Alfa Aesar, 98%) were dissolved in oleylamine (technical grade, Acros, 80%) by pumping for 16 h at 100 °C. The solution was then kept at 80 °C to avoid solidification. In a typical procedure, precursor with a 13.6:1 Cd:TDPA molar ratio was made by dissolving 0.30 g (1.64 mmol) of CdCl<sub>2</sub> and 0.033 g (0.12 mmol) of TDPA in 5 ml of oleylamine.

**Quantum dot synthesis and metal halide treatment.** PbS quantum dots were synthesized according to a previously published method<sup>35</sup>. For metal halide treatment, 1.0 ml metal halide precursor was introduced into the reaction flask after sulphur source injection during the slow cooling process. A 6:1 Pb:Cd molar ratio was maintained during the synthesis. When the reaction temperature reached 30–35 °C, the nanocrystals were isolated by the addition of 60 ml of acetone then centrifugation. The nanocrystals were then purified by dispersion in toluene and reprecipitation with acetone/methanol (1:1 volume ratio), then re-dissolved in anhydrous toluene. The solution was washed with methanol two or three more times before final dispersal in octane (50 mg ml<sup>-1</sup>).

**Photovoltaic device fabrication.** PbS CQD films were deposited using a layer-by-layer spin-coating process under an ambient atmosphere. For each layer, the CQD solution (50 mg ml<sup>-1</sup> in octane) was deposited on the ZnO/TiO<sub>2</sub> substrate and spin-cast at 2,500 r.p.m. In the hybrid and organic approaches, solid-state ligand exchange was performed by flooding the surface with 1% v/v MPA in methanol for 3 s before spin-coating dry at 2,500 r.p.m. Two washes with methanol were used to remove unbound ligands. Each device consisted of 8–12 layers. Inorganic-passivated devices were fabricated following the procedure described in ref. 12. Top electrodes were deposited using an Angstrom Engineering Åmod deposition system in an Innovative Technology glovebox. The contacts typically consisted of 10 nm thermally evaporated molybdenum trioxide deposited at a rate of 0.2 Å s<sup>-1</sup>, followed by electron-beam deposition of 50 nm of gold deposited at 0.4 Å s<sup>-1</sup>, and finally 120 nm of thermally evaporated silver deposited at 1.0 Å s<sup>-1</sup>.

**AM1.5 photovoltaic performance characterization.** Current–voltage data were measured using a Keithley 2400 source meter. The solar spectrum at AM1.5 was simulated to within class A specifications (less than 25% spectral mismatch) with a xenon lamp and filters (ScienceTech; measured intensity of 100 mW cm<sup>-2</sup>). The source intensity was measured with a Melles-Griot broadband power meter through a circular 0.049 cm<sup>2</sup> aperture at the position of the sample and confirmed with a calibrated reference solar cell (Newport). The accuracy of the current–voltage measurements was estimated to be ±7%.

**EQE measurements.** The EQE spectrum was obtained by passing the output of a 400 W xenon lamp through a monochromator and using appropriate order-sorting filters. The collimated output of the monochromator was measured through a 1 mm

aperture with calibrated Newport 818-UV and Newport 818-IR power meters as required. The beam was optically chopped and co-focused on the pixel with a solar simulator at 1-sun intensity. The measurement bandwidth was  $\sim 40$  nm and the intensity varied with the spectrum of the xenon lamp. The current response was measured with a Stanford Research Systems lock-in amplifier operating in current mode where a virtual null at the input approximates short-circuit conditions. The accuracy of the EQE measurements was estimated to be  $\pm 8\%$ .

**GISAXS.** GISAXS measurements were performed on Beamline 7.3.3 of the Advanced Light source (ALS) at Lawrence Berkeley National Laboratory. Monochromatic light was used with a wavelength of  $1.23984 \text{ \AA}$  (10 keV). The Pilatus 1M detector, a CMOS hybrid-pixel CCD camera with a pixel size of  $172 \mu\text{m} \times 172 \mu\text{m}$  and a total of  $981 \times 1,043$  pixels with a 20-bit dynamical range per pixel, was used to record the scattering patterns. Typical readout time per image was  $< 3.6$  ms. The images were dark-current-corrected, distortion-corrected and flat-field-corrected by the acquisition software. Using a silver behenate powder standard, the sample-to-detector distance was determined to be  $1,350.74$  or  $1,356.84$  mm. The angle of incidence of the X-ray beam was varied between  $0.02$  and  $0.15^\circ$ . Typical exposure times ranged from  $20$  to  $300$  s. All three films shown in Fig. 3 were made from the same QCDs treated with  $\text{CdCl}_2$  during synthesis; the only difference was in the film-forming solid-state exchange procedure. All show primarily ring-like GISAXS patterns. We plotted azimuthally integrated intensity profiles<sup>35</sup> (Fig. 3d) and used Gaussian fitting plus an exponential background to determine the location of the scattering rings at  $q \approx 0.2 \text{ \AA}^{-1}$ . Conversion to real-space coordinates gave average centre-to-centre nanocrystal spacings of  $4.37$ ,  $4.48$  and  $3.36$  nm for the unexchanged, inorganic and hybrid films, respectively.

**TOF method.** This method<sup>33</sup> was used to measure hole carrier mobility. TOF experiments were carried out on samples with a geometry identical to that of the photovoltaic device, with the exception that the total nanocrystal layer in this case was thicker ( $> 500$  nm). The samples were excited using a diode-pumped passively Q-switched solid-state laser operating at  $355$  nm with  $1$  ns pulses at a  $200$  Hz repetition rate. The light was incident on the sample from the transparent FTO side. The devices were biased using a Keithley 228 voltage/current source, and a digital Tektronix TDS5104 oscilloscope was used to measure the current transient output across a  $50 \Omega$  load.

Received 14 May 2012; accepted 22 June 2012;  
published online 29 July 2012

## References

- Kramer, I. J. & Sargent, E. H. Colloidal quantum dot photovoltaics: a path forward. *ACS Nano* **5**, 8506–8514 (2011).
- Pattantyus-Abraham, A. G. *et al.* Depleted-heterojunction colloidal quantum dot solar cells. *ACS Nano* **4**, 3374–3380 (2010).
- Wang, X. *et al.* Tandem colloidal quantum dot solar cells employing a graded recombination layer. *Nature Photon.* **5**, 480–484 (2011).
- Semonin, O. E. *et al.* Peak external photocurrent quantum efficiency exceeding 100% via MEG in a quantum dot solar cell. *Science* **334**, 1530–1533 (2011).
- Kramer, I. J., Levina, L., Debnath, R., Zhitomirsky, D. & Sargent, E. H. Solar cells using quantum funnels. *Nano Lett.* **11**, 3701–3706 (2011).
- Schaller, R. & Klimov, V. High efficiency carrier multiplication in PbSe nanocrystals: implications for solar energy conversion. *Phys. Rev. Lett.* **92**, 186601 (2004).
- Gur, I., Fromer, N. A., Geier, M. L. & Alivisatos, A. P. Air-stable all-inorganic nanocrystal solar cells processed from solution. *Science* **310**, 462–465 (2005).
- Luther, J. M. *et al.* Structural, optical, and electrical properties of self-assembled films of PbSe nanocrystals treated with 1,2-ethanedithiol. *ACS Nano* **2**, 271–280 (2008).
- Law, M. *et al.* Structural, optical, and electrical properties of PbSe nanocrystal solids treated thermally or with simple amines. *J. Am. Chem. Soc.* **130**, 5974–5985 (2008).
- Koleilat, G. I. *et al.* Efficient, stable infrared photovoltaics based on solution-cast colloidal quantum dots. *ACS Nano* **2**, 833–840 (2008).
- Beard, M. C. *et al.* Variations in the quantum efficiency of multiple exciton generation for a series of chemically treated PbSe nanocrystal films. *Nano Lett.* **9**, 836–845 (2009).
- Tang, J. *et al.* Colloidal-quantum-dot photovoltaics using atomic-ligand passivation. *Nature Mater.* **10**, 765–771 (2011).
- Yu, M. *et al.* First principles study of CdSe quantum dots: stability, surface unsaturations, and experimental validation. *Appl. Phys. Lett.* **88**, 231910 (2006).
- Voznyy, O. Mobile surface traps in CdSe nanocrystals with carboxylic acid ligands. *J. Phys. Chem. C* **115**, 15927–15932 (2011).
- Owen, J. S., Park, J., Trudeau, P.-E. & Alivisatos, A. P. Reaction chemistry and ligand exchange at cadmium-selenide nanocrystal surfaces. *J. Am. Chem. Soc.* **130**, 12279–12281 (2008).
- Mocatta, D. *et al.* Heavily doped semiconductor nanocrystal quantum dots. *Science* **332**, 77–81 (2011).
- Fu, H. *et al.* Impact of the growth conditions of colloidal PbS nanocrystals on photovoltaic device performance. *Chem. Mater.* **23**, 1805–1810 (2011).
- Nag, A. *et al.* Metal-free inorganic ligands for colloidal nanocrystals:  $\text{S}^{2-}$ ,  $\text{HS}^-$ ,  $\text{Se}^{2-}$ ,  $\text{HSe}^-$ ,  $\text{Te}^{2-}$ ,  $\text{HTe}^-$ ,  $\text{TeS}_3^{2-}$ ,  $\text{OH}^-$ , and  $\text{NH}_2^-$  as surface ligands. *J. Am. Chem. Soc.* **133**, 10612–10620 (2011).
- Tang, J. *et al.* Quantum dot photovoltaics in the extreme quantum confinement regime: the surface-chemical origins of exceptional air- and light-stability. *ACS Nano* **4**, 869–878 (2010).
- Galland, C. *et al.* Two types of luminescence blinking revealed by spectroelectrochemistry of single quantum dots. *Nature* **479**, 203–207 (2011).
- Liu, Y. *et al.* Dependence of carrier mobility on nanocrystal size and ligand length in PbSe nanocrystal solids. *Nano Lett.* **10**, 1960–1969 (2010).
- Nagpal, P. & Klimov, V. I. Role of mid-gap states in charge transport and photoconductivity in semiconductor nanocrystal films. *Nature Commun.* **2**, 486 (2011).
- Shuttle, C. G. *et al.* Experimental determination of the rate law for charge carrier decay in a polythiophene: fullerene solar cell. *Appl. Phys. Lett.* **92**, 093311 (2008).
- O'Regan, B. C., Scully, S., Mayer, A. C., Palomares, E. & Durrant, J. The effect of  $\text{Al}_2\text{O}_3$  barrier layers in  $\text{TiO}_2$ /dye/CuSCN photovoltaic cells explored by recombination and DOS characterization using transient photovoltage measurements. *J. Phys. Chem. B* **109**, 4616–4623 (2005).
- Liu, H. *et al.* Electron acceptor materials engineering in colloidal quantum dot solar cells. *Adv. Mater.* **23**, 3832–3837 (2011).
- Moreels, I. *et al.* Size-dependent optical properties of colloidal PbS quantum dots. *ACS Nano* **3**, 3023–3030 (2009).
- Ito, S. *et al.* Control of dark current in photoelectrochemical ( $\text{TiO}_2/\text{I}^-/\text{I}_3^-$ ) and dye-sensitized solar cells. *Chem. Commun.* 4351–4353 (2005).
- Huang, N. *et al.* Synergistic effects of ZnO compact layer and  $\text{TiCl}_4$  post-treatment for dye-sensitized solar cells. *J. Power Sources* **204**, 257–264 (2012).
- Yong, K.-T., Sahoo, Y., Swihart, M. T. & Prasad, P. N. Shape control of CdS nanocrystals in one-pot synthesis. *J. Phys. Chem. C* **111**, 2447–2458 (2007).
- Heitsch, A. T., Patel, R. N., Goodfellow, B. W., Smilgies, D.-M. & Korgel, B. A. GISAXS characterization of order in hexagonal monolayers of FePt nanocrystals. *J. Phys. Chem. C* **114**, 14427–14432 (2010).
- Jiang, Z., Lin, X.-M., Sprung, M., Narayanan, S. & Wang, J. Capturing the crystalline phase of two-dimensional nanocrystal superlattices in action. *Nano Lett.* **10**, 799–803 (2010).
- Hanrath, T., Choi, J. J. & Smilgies, D.-M. Structure/processing relationships of highly ordered lead salt nanocrystal superlattices. *ACS Nano* **3**, 2975–2988 (2009).
- Naka, S., Okada, H., Onnagawa, H. & Tsutsui, T. High electron mobility in bathophenanthroline. *Appl. Phys. Lett.* **76**, 197–199 (2000).
- Kalyuzhny, G. & Murray, R. W. Ligand effects on optical properties of CdSe nanocrystals. *J. Phys. Chem. B* **109**, 7012–7021 (2005).
- Hines, M. A. & Scholes, G. D. Colloidal PbS nanocrystals with size-tunable near-infrared emission: observation of post-synthesis self-narrowing of the particle size distribution. *Adv. Mater.* **15**, 1844–1849 (2003).

## Acknowledgements

This publication is based in part on work supported by an award (KUS-11-009-21) from the King Abdullah University of Science and Technology (KAUST), by the Ontario Research Fund Research Excellence Program and by the Natural Sciences and Engineering Research Council (NSERC) of Canada. The authors thank Angstrom Engineering and Innovative Technology for useful discussions regarding material deposition methods and control of the glovebox environment, respectively. The Advanced Light Source is supported by the Director, Office of Science, Office of Basic Energy Sciences, of the US Department of Energy (contract no. DE-AC02-05CH11231). The authors thank L. Goncharova, M. T. Greiner, E. Palmiano, R. Wolowiec and D. Kopilovic for their help during the course of the study. A.H.I. acknowledges support from the Queen Elizabeth II Graduate Scholarship in Science and Technology. D.Z. acknowledges support from the NSERC CGS D scholarship.

## Author contributions

A.H.I., S.M.T. and E.H.S. designed and directed this study and analysed the experimental results. A.H.I. and S.M.T. contributed to all the experimental work. S.H. and D.Z. carried out the photovoltage transient measurements. S.H. performed PLQE experiments. O.V. performed DFT, RBS and XPS analyses. D.Z. performed the optoelectronic simulations. R.D. assisted in conceptualization of the study and assisted in experimental work. L.L. synthesized the QCDs. L.R.R., K.W.C. and A.A. carried out the GISAXS measurements. G.H.C. performed the TOF measurements. A.F. performed XPS and CHN analyses. K.W.K. performed TAS and capacitance–voltage measurements. I.J.K. assisted with EQE measurements. Z.N. developed protocols for the separation of treatment constituents experiment and facilitated ICP AES measurements. A.J.L. assisted with device fabrication and testing. A.H.I., S.M.T. and E.H.S. wrote the manuscript. All authors commented on the paper.

## Additional information

Supplementary information is available in the online version of the paper. Reprints and permission information is available online at <http://www.nature.com/reprints>. Correspondence and requests for materials should be addressed to E.H.S.

## Competing financial interests

The authors declare no competing financial interests.